Computers in Biology and Medicine 164 (2023) 107364

Contents lists available at ScienceDirect

Computers in Biology and Medicine

journal homepage: www.elsevier.com/locate/compbiomed

Digital image analysis workflows for evaluation of cell behavior and tumor microenvironment to aid therapeutic assessment in high-risk neuroblastoma

M. Stoks [a], I. Vieco-Martí [a,b], I. Noguera [a,c], M. Sánchez-Sánchez [b], R. Burgos-Panadero [a,b], S. Navarro [a,b], R. Noguera [a,b,*]

[a] CIBERONC, Carlos III Health Institute (Ministry of Economy and Competitiveness), 28029, Madrid, Spain
[b] Department of Pathology, Medical School, University of Valencia - INCLIVA Biomedical Health Research Institute, 46010, Valencia, Spain
[c] Central Support Service for Experimental Research (SCSIE), University of Valencia, Burjassot, Valencia, Spain

ARTICLE INFO

Keywords:
Digital pathology
Extracellular matrix
Preclinical therapeutic studies
Vitronectin
Cilengitide

ABSTRACT

Digital pathology and artificial intelligence are promising emerging tools in precision oncology as they provide more robust and reproducible analysis of histologic, morphologic and topologic characteristics of tumor cells and the surrounding microenvironment. This study aims to develop digital image analysis workflows for therapeutic assessment in preclinical in vivo models. For this purpose, we generated pipelines that enable automatic detection and quantification of vitronectin and αvβ3 in heterotopic high-risk neuroblastoma xenografts, demonstrating that digital analysis workflows can be used to provide robust detection of vitronectin secretion and αvβ3 expression by malignant neuroblasts and to evaluate the possibility of combining traditional chemotherapy (etoposide) with extracellular matrix-targeted therapies (cilengitide). Digital image analysis added evidence for the relevance of territorial vitronectin as a therapeutic target in neuroblastoma, since its expression is modified after treatment, with a mean percentage of 60.44% in combined therapy tumors vs 45.08% in control ones. In addition, the present study revealed the efficacy of cilengitide for reducing αvβ3 expression, with a mean αvβ3 positivity of 34.17% in cilengitide treated material vs 66.14% in control and with less tumor growth when combined with etoposide, with a final mean volume of 0.04 cm^3 in combined therapy vs 1.45 cm^3 in control. The results of this work highlight the importance of extracellular matrix-focused therapies in preclinical studies to improve therapeutic assessment for high-risk neuroblastoma patients.

1. Introduction

The extracellular matrix (ECM) is a fundamental component of the tumor microenvironment (TME), where it has crucial role in tumor progression and metastasis, providing not only scaffolding for cells but also biochemical and biomechanical signals that promote cell growth, migration and differentiation [1,2]. Vitronectin (VN) is a glycoprotein present in the ECM capable of interacting with different cell receptors and other macromolecules of the ECM. During recent years, VN has gained special interest in cancer research as it promotes cell adhesion to the ECM and participates in cell differentiation, migration and proliferation through interaction with integrins (αvβ3, αvβ5, αvβ1, αIIbβ3, αvβ6 and αvβ8), urokinase-type plasminogen activator receptor (uPAR) and plasminogen activator inhibitor-1 (PAI-1) [3–6]. VN is present in plasma and the ECM of different human tissues. It is mainly synthesized by hepatocytes, although increased depositions have been described in various cancerous tissues, suggesting VN production by extrahepatic cells in diseased tissue [3,4]. It has been observed that some tumor cells, such as glioma cells, ovarian adenocarcinoma cells and colorectal adenocarcinoma cells, are able to synthesize and secrete VN [7–9].

Neuroblastoma (NB) is the most common extracranial solid tumor in children and is characterized by intertumoral biological and clinical heterogeneity [10,11]. Previous studies carried out by our group have demonstrated in vitro and in vivo VN secretion by malignant neuroblasts. In particular, positive VN expression has been observed in monolayer cell cultures of SK-N-BE (2) and SH-SY5Y, among other NB cell lines [12]. In addition to the in vitro models, orthotopic high-risk NB (HR-NB) xenografts generated using SH-SY5Y and SK-N-BE (2) cells

* Corresponding author. CIBERONC, Carlos III Health Institute (Ministry of Economy and Competitiveness), 28029, Madrid, Spain.
E-mail address: rnoguera@uv.es (R. Noguera).

https://doi.org/10.1016/j.compbiomed.2023.107364
Received 7 June 2023; Received in revised form 3 August 2023; Accepted 12 August 2023
Available online 14 August 2023

lines in VN-knock out (VN–KO) mice have revealed that malignant neuroblasts growing in a TME secrete VN analogously to human NB tumors [13], demonstrating that VN synthetized by neuroblastic cells is an important ECM glycoprotein in aggressive NB. Moreover, digital pathology image analysis revealed two VN expression patterns: territorial VN, which is recently incorporated VN with an intra- or pericellular location; and interterritorial VN, which is intercellular VN integrated into the ECM earlier on [13].

Digital pathology is emerging as a robust, fast and efficient tool to identify and analyze histologic and morphologic characteristics of whole slide images (WSIs) for pathological changes [14]. Greater cost efficiency and technological progress in image acquisition and analysis have made WSIs the future standard for digital pathology and clinical diagnostics, allowing rapid, simultaneous study of multiple samples and stains [15]. Digital analysis tools have proven useful for the analysis of topological and morphometric characteristics representative of cancer, optimizing the accuracy of disease diagnosis, grading and prognosis [16]. Our group has focused on the ECM in NB tumors to discover new features that could enable more precise prognosis and risk stratification. Using digital pathology tools, we have defined the topology and/or morphometric features of lymphatic and blood vessels and several ECM components (VN, reticulin fibers, elastic fibers, collagen type I fibers and glycosaminoglycans) [13,17,18].

The high heterogeneity of NB has hindered the development of a successful treatment for high-risk NB (HR-NB), with survival rates ranging from >90% for patients with non-HR-NB to <50% for patients with HR-NB [19]. Several novel ECM-targeted therapies, especially for HR patients, have emerged in response to this issue. Integrin inhibitors have been proposed as therapeutic agents, as they are key receptors which communicate with the ECM [20,21]. Cilengitide (CLG) is a cyclic pentapeptide that blocks αvβ3 and αvβ5 integrins from binding to the arginine-glycine-aspartate (RGD) sequence of several ECM proteins such as fibronectin and VN [22], although unfavorable pharmacokinetics have prevented it from reaching the market as yet [23]. Preclinical therapeutic studies by our group have shown that CLG has direct anticancer activity in six different HR-NB cell lines and presented synergy with free and nano-encapsulated etoposide (ETP) in SK-N-BE (2) monolayer cell cultures [12].

In this work, we used digital pathology workflows for topological and spatial analysis of VN and αvβ3 in heterotopic HR-NB xenografts treated with ETP alone, CLG alone or CLG combined with ETP. We subsequently assessed the tumor growth rate to determine whether these treatments could serve as growth containment. The digital image analyses carried out herein prove the importance of digital pathology in the study of topologic and histopathologic features of ECM components of NB to aid objective disease diagnosis and preclinical therapeutic assessment.

2. Materials and methods

2.1. Heterotopic xenografts

Heterotopic HR-NB xenografts were generated using the SK-N-BE (2) cell line in RAG1−/− and VN−/− female or male mice. The cell line was purchased from the ATCC (American Type Culture Collection). The SK-N-BE (2) cell line was grown under 5% CO2 at 37 °C and maintained in Iscove's Modified Dulbecco's Medium (IMDM) supplemented with 10% heat-inactivated fetal bovine serum (FBS), 1% insulin-transferrin-selenium (ITS) and 100 U/mL of penicillin/100 μg/mL streptomycin. All reagents were obtained from Gibco, Thermo Fisher Scientific Inc., Waltham, MA, USA. When RAG1−/− VN−/− animals were around four to six weeks old, subcutaneous HR-NB xenografts were generated by inoculating $2x10^6$ cells from the SK-N-BE (2) cell line.

For the first thirty days after inoculation, tumor progress was evaluated weekly by measuring its dimension with Vernier caliper and using the formula: $V = (\pi \cdot l \cdot s^2)/6$ mm^3, where l refers to length and s to width. All experiments were carried out in accordance with the standards and care approved by the Institutional Animal Care Ethics Committee (reference 2021/VSC/PEA/0052). Additional information on experimental procedures and animal care is available in Appendix A.

2.2. Treatment

ETP powder (Etoposide synthetic, 98.0–105.0%, powder, E1383-250 MG, Merck) was dissolved in dimethyl sulfoxide (DMSO) [Sigma-Aldrich] to obtain a stock solution of 50 mg/mL. For mice inoculation, aliquots with a final concentration of 2 mg/mL were prepared from the stock solution using 0.9% saline serum as dissolvent. CLG powder (Cilengitide trifluoroacetic acid salt ≥98% (HPLC), SML1594-25 MG, Merck) was dissolved in 0.9% saline serum and homogenized by vortex, obtaining a solution of 4 mg/mL. The dose for each drug (ETP and CLG) was 20 mg/kg mouse body weight. Animals received the treatment three times per week for two weeks. On the day of administration, animals were weighed and the amount of solution to be injected was calculated. Both ETP and CLG were administrated with an intraperitoneal injection. In the case of controls, 200 μL of 0.9% saline serum were intraperitoneally injected.

2.3. Sample processing and digitization

Collected heterotopic HR-NB xenografts (n = 16) were fixed by immersion in 4% paraformaldehyde (PFA) and automatically embedded in paraffin. After processing, paraffin blocks were assembled and cut into 3-μm sections. VN and αvβ3 staining were performed for digital image analysis of the sections, using the following antibodies: anti-VN (1/100, ab45139, Abcam) and anti-αvβ3 (1/50, ab7166, Abcam). Automated antigen retrieval (PT Link equipment, Dako, Glostrup, Denmark) and immunostaining (Autostainer Link 48 automated immunostaining machine, Dako, Glostrup, Denmark) were performed. VN and αvβ3 stained sections were digitalized as whole slide images using a Ventana iScan HT (Roche, Switzerland) at 20x magnification.

2.4. Center and periphery determination of samples

To determine VN expression patterns, the center and periphery of samples were determined with a digital pathology workflow. The whole pipeline is represented in Fig. 1. All steps were carried out with the aid of QuPath [24]. First, the image was split if the subcutaneous xenograft had more than one fragment so that each tissue fragment was exported to a separate image file. After tumor detection, 75 μm of the sample edge was removed when needed to avoid false positive diaminobenzidine (DAB) reactions. Next, the center and periphery of the samples were differentiated according to their solidity (area/convex area) so that both represented approximately fifty percent of the tumor area. Samples not fulfilling this condition were further analyzed according to different morphologic features (examples in Fig. S1). The center and periphery of samples with a solidity under 0.7 were established according to tumor size; for tumors that presented an area <1 mm^2, the boundary was buffered 50 μm inward while the boundary of tumors >1 mm^2 was buffered 100 μm inward. Tumors with solidity higher than 0.7 were dilated 100 μm outward and 100 μm inward. After two consecutive dilations, the center and periphery of these samples were differentiated according to their solidity as previously described. The scripts generated and used are available in Appendix B.

2.5. Digital image analysis

For both VN and αvβ3, analyses were performed using QuPath [24]. All steps are represented in Figs. 2 and 3. VN was quantified to assess whether the drugs had an effect on VN secretion. We also evaluated whether VN expression was affected by tumor area (center/periphery). For each section fragment, tumor tissue was automatically detected in

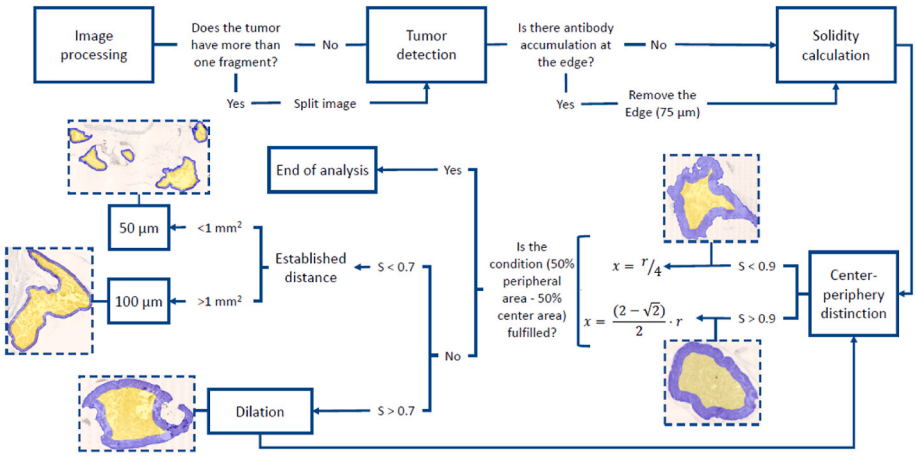

Fig. 1. Pipeline overview of how center and periphery were defined. The proposed approach can differentiate the center and periphery of the samples according to area and/or solidity (area/convex area). Solidity gives a measure of the compactness of the tumor. S: solidity; x: width of the periphery ring; r: sample minimum radius. More information available in Fig. S2.

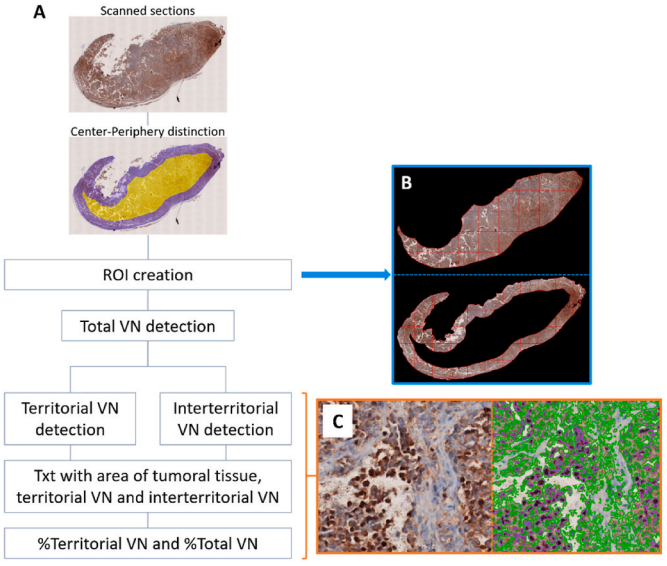

Fig. 2. Representative images of scanned sections and digital pathology workflow overview for VN analysis. The process starts with distinction of the center and the periphery of the stained histology sections (A), followed by the creation of 1000 × 1000 µm^2 ROIs (B) and detection of total VN, territorial VN (purple) and interterritorial VN (green) (C). ROI: region of interest; txt: text file.

QuPath with the 'Thresholding function'; all pixels with scores below 170 were thresholded to determine tumor tissue. Additional information about the settings used for tumor tissue detection are available at Table S1. Next, the center and periphery of the sections were differentiated (Fig. 2A) as previously described. When needed, areas of necrosis and folds or other artifacts were manually removed. Due to the size of the whole slide histology images, the detected tumor was automatically fractionated into ROIs (regions of interest) of 1000 × 1000 µm^2 to aid VN detection (Fig. 2B) with the corresponding script (Appendix B). For each ROI, VN was automatically identified and territorial VN and interterritorial VN were distinguished according to pixel color and intensity, applying several artificial neural network classifiers to train QuPath interactively to distinguish territorial and interterritorial VN (Fig. 2C); territorial VN location was represented by strongly stained intensity and interterritorial VN location by low and medium intensity. A corresponding script (Appendix B) was designed to run on all histology images to automate territorial VN and interterritorial VN detection; the parameters required for VN detection are shown in Table S2.

A different approach was used for αvβ3 analysis (Fig. 3). For each histology image (Fig. 3A), tumor tissue was classified using the 'Thresholding function' in QuPath; all pixels with scores below 200 were classified as tumor tissue (Fig. 3B). Areas of necrosis and folds or other artifacts were manually removed when necessary. Next, αvβ3 detection was automated with the 'Positive cell detection function' in QuPath (Fig. 3C). A corresponding script was then generated to run on all histology images (Appendix B), thereby automating αvβ3-positive cell detection. Cells with positivity for αvβ3 were defined by cells with an optical density (OD) of the DAB color greater than 0.3 in the nucleus. More details about the settings used for tumor tissue and positive cell detection are available at Table S1 and Table S3, respectively.

3. Results

3.1. Vitronectin expression by neuroblastic cells in HR-NB heterotopic xenografts

VN expression was evaluated in neuroblastic cells with antibody anti-VN on 16 histological images taken from subcutaneous HR-NB xenografts. Using digital image analysis, we observed positive VN detection in all samples (Fig. 4). In addition, we were able to distinguish two VN expression patterns as described in above mentioned articles and previous studies [12,13,18].

VN was objectively quantified as the percentage of territorial, interterritorial and total VN stained area. Unexpectedly, %territorial VN (Fig. 5A) and %total VN (Fig. 5B) were higher in all treatment groups (ETP alone, CLG alone, and the two drugs in combination) than in the control group, where no treatment was used (Fig. 5). Statistical analysis of the VN expression results was carried out, but due to the dispersion of data and the low number of samples (Fig. 5), no statistically significant results were obtained.

3.2. Vitronectin distribution (center/periphery)

Given the utility of topological distribution of biomolecules to improve understanding of the behavior of tumoral cells in its microenvironment, we next evaluated VN disposition in the samples. Using the designed pipeline, we distinguished the center and periphery of the samples and analyzed VN distribution in those regions. VN was detected equally in the center and the periphery in most samples (Fig. 6). The biggest difference could be seen in the quantification of territorial VN in the center and periphery of the group treated with the combination of ETP and CLG (Fig. 6A and B).

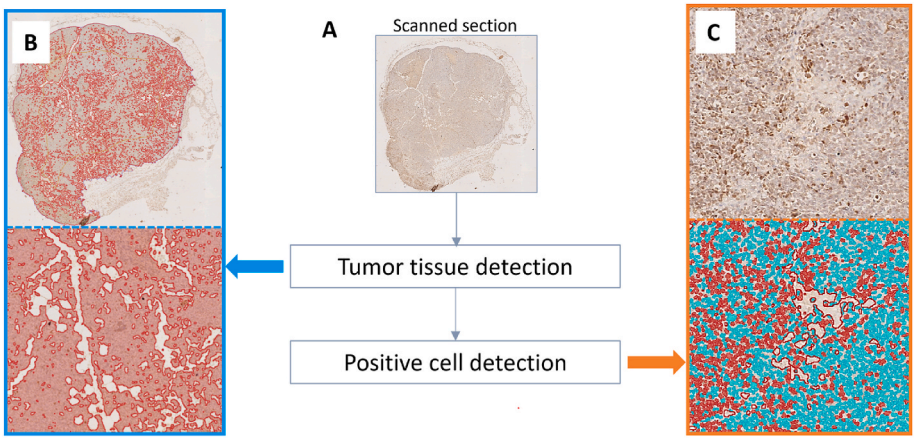

Fig. 3. Digital image analysis workflow for αvβ3 positivity study. (A) Scanned tissue section. (B) Representative pictures of tumor tissue detection (in red) using the 'Thresholding function' in QuPath. (C) Representative pictures of positive cell detection on αvβ3 stained histology sections with 'Positive cell detection function' in QuPath; red cells are positive and blue cells are negative.

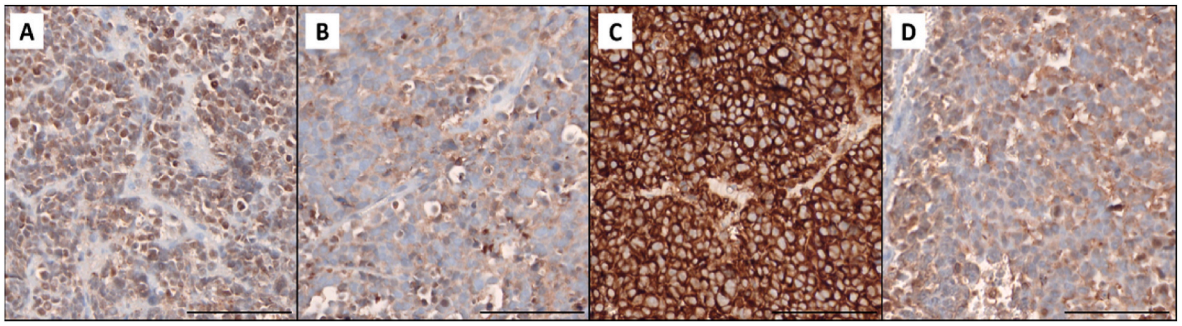

Fig. 4. Vitronectin expression by neuroblastic cells in non-treated HR-NB heterotopic xenografts (A) and HR-NB heterotopic xenografts treated with ETP (B), CLG (C), and ETP and CLG (D). Scale bar: 100 μm. ETP: etoposide; CLG: cilengitide.

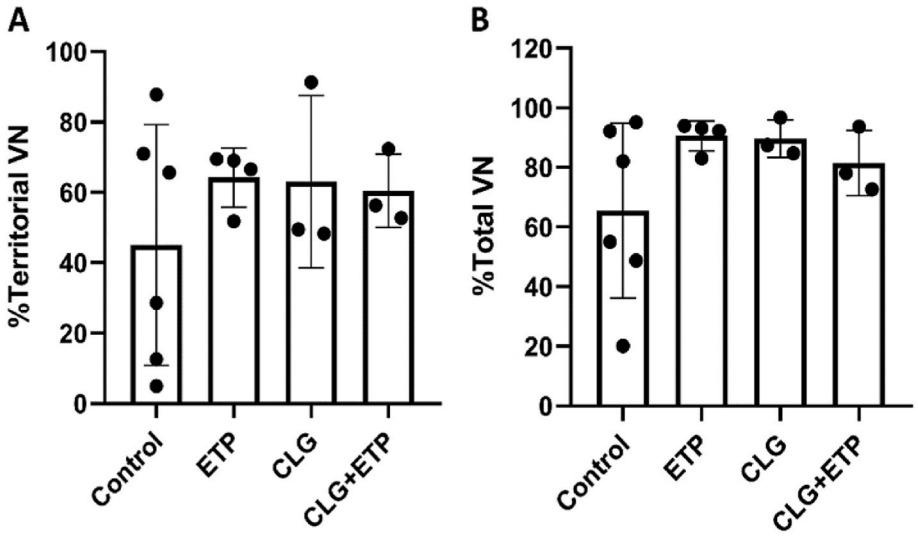

Fig. 5. Quantification of territorial vitronectin (VN) (A) and total VN (B) secreted by neuroblastic SK-N-BE (2) cells in control group and samples treated with ETP, CLG alone and CLG combined with ETP. The percentage of territorial VN and total VN are represented in the graphs as area of territorial VN and total VN, respectively, relative to the total sample area. The graphs represent mean ± standard deviation (SD) of at least three values (Table S4); the number of values is represented by the dots. ETP: etoposide; CLG: cilengitide.

Quantification of territorial VN (Fig. 6B) and total VN (Fig. 6D) revealed no significant differences in VN expression between the center and the periphery of the subcutaneous xenografts. Interestingly, the same tendency was observed in both the center and the periphery; % territorial VN (Fig. 6A) and %total VN (Fig. 6C) was greater in treated samples than the control group, regardless of whether ETP alone, CLG alone or CLG in combination with ETP was used.

3.3. αvβ3 expression in HR-NB heterotopic xenografts

To assess αvβ3 expression by neuroblastic cells, we analyzed 13 histological images taken from subcutaneous HR-NB xenografts stained with anti- αvβ3. As previously mentioned we used an automated digital image analysis pipeline based on the intensity and colors of the pixels for this purpose, observing positive αvβ3 expression in all samples (Fig. 7).

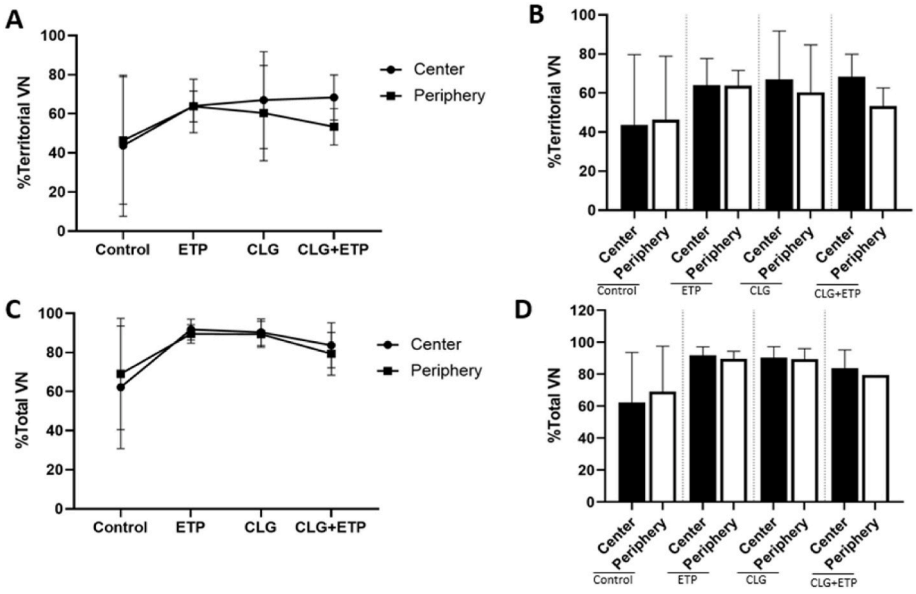

Fig. 6. Distribution of territorial and total vitronectin (VN) in control and treatment groups. (A,B) Territorial VN secretion in center and periphery of the different treatment groups. The graphs represent mean ± SD of at least three values. (C,D) Total VN secretion in center and periphery of the different treatment groups. The graphs represent mean ± SD of at least three values (Table S4). ETP: etoposide; CLG: cilengitide.

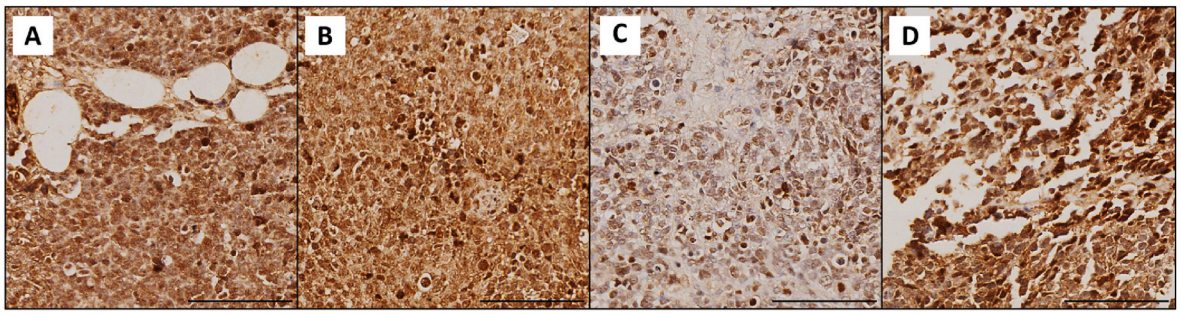

Fig. 7. αvβ3 expression by neuroblastic cells in non-treated HR-NB heterotopic xenografts (A) and HR-NB heterotopic xenografts treated with ETP (B), CLG (C), and ETP and CLG (D). Scale bar: 100 μm. ETP: etoposide; CLG: cilengitide.

Although no statistically significant differences were found, the samples treated with CLG alone had lower average αvβ3 detection than the controls or other treatment groups [ETP alone or in combination with CLG] (Fig. 8A). To assess the possible relationship between αvβ3 expression and territorial VN secretion in HR-NB, the percentage of expression of the two proteins was measured, as illustrated in Fig. 8B. As previously described, VN synthesis was higher but not statistically significant in all treatment groups compared with the control group. In contrast, αvβ3 detection was lower in the CLG group than the control group or two remaining treatment groups (ETP alone and in combination with CLG).

3.4. Cellular response to cilengitide

All treatment groups and controls presented a similar growth pattern; tumor volume increased over time (Fig. 9A1,A2), even though

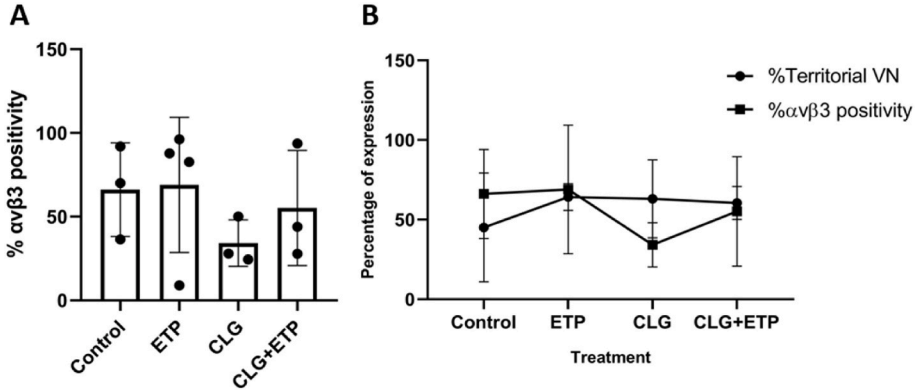

Fig. 8. (A) Immunohistochemistry quantification of αvβ3 expression by neuroblastic cells. The percentage of αvβ3 is represented in the graph as number of positive cells relative to the total cell number. The number of samples is represented by dots. (B) Percentage of expression of territorial VN and αvβ3 positivity in control and treatment groups (ETP, CLG, CLG and ETP). Values are the mean ± standard deviation (SD) of at least three independent determinations (Table S5). VN: vitronectin; ETP: etoposide; CLG: cilengitide.

three groups underwent treatment. Despite the lack of significant differences, the tumor volume reached in the treatment groups was lower than in the control group. In this regard, both CLG and ETP exerted a moderate influence on tumor growth, with a stronger effect in combination. Tumor growth pattern (Fig. 9A1,A2) shows that final tumor volume was considerably lower after combined treatment (CLG with ETP) than in the remaining groups.

To confirm whether the treatments served as growth containment, HR-NB heterotopic xenografts were collected after the last treatment dose, and final tumor volume was digitally calculated (Fig. 9B). Digital measurements revealed greater volumes in the control group (which had not undergone any treatment) than the treatment groups. Concerning the latter, Fig. 9B shows that combining CLG and ETP achieved lower average volume and dispersion data than individual treatments. These results suggest that the combination of CLG with ETP enhances tumor growth containment. However, no statistical between-group differences could be inferred.

4. Discussion

Digital pathology techniques improve quantitative accuracy and guarantee standardized measurement of histological features and morphological patterns [25]. Among their range of applications, these techniques can be used to gain insight into ECM composition and its complex interaction with the surrounding cells, revealing novel biomarkers for cancer diagnostics or grading and potential drug targets [26,27]. The digital analysis workflows generated in the present study enable efficient and standardized detection of VN (an important cell-secreted glycoprotein) and αvβ3 (a key cell receptor), minimizing inter- and intra-observer differences. Although no significant differences were found in VN distribution, the addition of spatial metrics could potentially improve the clinical value of this biomarker [26]. We have demonstrated that image analysis workflows can be generated to robust detection of VN secretion and αvβ3 expression by malignant neuroblasts and to evaluate the possibility of combining traditional chemotherapy with ECM-targeted therapies.

With the rise of digital pathology tools and an increased focus on precision medicine, identifying novel biomarkers to improve patient stratification has also gained interest, to help tailor medical treatments more precisely to the characteristics of a patient subgroup [28]. In this regard, several research groups have identified TME components that may serve as potential diagnostic and/or prognostic biomarkers [29–31]. Although NB patients are stratified into pretreatment groups according to several clinical, biological and genetic markers to improve treatment strategies [32], children with HR-NB currently have a long-term survival rate of around 50% [33]. As reported by our group, quantifying TME components through standardized digital image analysis techniques is an effective tool for enhancing patient risk stratification, and by extension offering new therapeutic opportunities [18]. Our research showed that among various ECM elements, VN may contribute more than was previously thought to prognostic assessment of patients affected by NB. Findings have indicated that territorial VN is relevant to evaluate NB patient risk groups; higher territorial VN was detected in human tumors with unfavorable histology and was related to unfavorable independent prognostic INRG variables [13,17]. Regarding the importance of digital pathology and VN, several studies have shown that VN quantification can be used as a diagnostic and/or prognostic predictor for human glioma, breast cancer, osteosarcoma, melanoma and gastric cancer [34–38]. The present work reinforces the potential utility of standardized digital detected territorial VN for NB prognosis.

We have already outlined that a diverse range of TME components can be used as tumor biomarkers; however, recent studies have explored the importance not only of the density or intensity of biomarkers, but also of their distribution within the tissue [39–41]. In this regard, some studies have revealed that geometric tools can be used to distinguish between healthy and unhealthy tissue [42–44]. It is within our scope to use the present pipelines to develop ground truth masks and train artificial intelligence models, with the aim of further examining the potential of these ECM components and their spatial analysis as supplementary biomarkers. As described in previous publications, VN and its interaction with the αvβ3 integrin is clinically relevant in HR-NB poor prognosis [12], making VN and its ligands useful therapeutic targets. The main therapeutic aim would be to reduce VN secretion by malignant neuroblasts or inhibit their interaction with VN through αvβ3 to modulate the relationship between the cells and the ECM. Prior preclinical studies by our group showed that CLG possesses anticancer

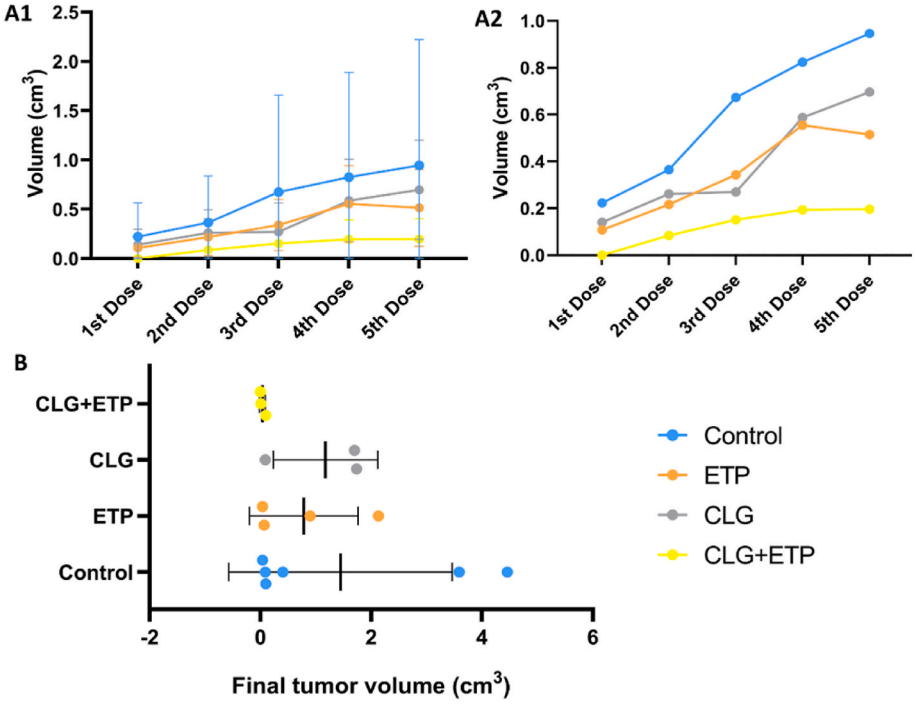

Fig. 9. Tumor volume measurements after treatment administration. Tumor volume was measured with Vernier caliper (A) or by using digital image analysis (B). (A) Tumor volume measurements after administration of five 20 mg/kg doses of ETP, CLG or ETP and CLG. A1 represents mean ± SD of at least three values while A2 represents the mean of at least three values (Table S6A). (B) Scatterplot of tumor volume measurements after the last treatment dose administration. Values are mean ± SD (Table S6B). ETP: etoposide; CLG: cilengitide.

properties, effectively reducing cell viability of in vitro HR-NB VN-secreted cells, although they are independent from αvβ3 integrin expression in pre-treatment HR-NB cells, as observed using optical subjective quantification [12]. Our present image analysis results, although not statistically significant, show that CLG reduces αvβ3 detection in heterotopic HR-NB xenografts compared to ETP or no treatment. The reduced αvβ3 expression is outlined in the proposal of Sancey et al. [45], who in a study of αvβ3 integrin clustering and internalization developed a template with four cyclic RGD motifs capable of targeting αvβ3 in vitro and in vivo through internalization, mainly via clathrin-mediated endocytosis. This reinforces the value both of CLG as a therapeutic agent and of cell receptor quantification by digital analysis. Interestingly, we also found that VN secretion and incorporation into the ECM was slightly (but not statistically significantly) higher in all treatment groups than the control group. As previously described by Edwards et al. [46], recently synthesized VN incorporated into the ECM could converge with the formation of pathways promoting cell migration in an αvβ3-independent manner. However, CLG effectiveness is thought to result from αvβ3 and αvβ5 blocking affecting signaling pathways involved in cell adhesion, survival and proliferation, and thus inducing cell detachment from the surrounding ECM and decreasing cell proliferation [25]. Indeed, in a study in NB and glioma cell lines, CLG had a dose-dependent cytotoxicity effect on αvβ3-and αvβ5-expressing cell lines due to its capacity to induce cell detachment, ultimately leading to cell growth inhibition [47]. Our results show that both ETP and CLG are capable of containing tumor growth individually, but have a remarkably stronger effect when combined, suggesting that their combination is able to increase HR-NB treatment effectiveness by simultaneously targeting the tumoral cell and the surrounding ECM [48], as described in previous studies [12]. The main limitation of the present study is the relatively small sample size; this likely explains the greater than expected dispersion in data, which prevented us from obtaining a significant statistic to support our results. Larger-scale studies are required to improve understanding of the role of VN and its ligands in NB aggressiveness and the cellular effects of CLG on αvβ3 expression and VN secretion by neuroblastic cells. However, the results add evidence supporting the validity of VN as a therapeutic target in NB, warranting future studies with an increased sample size.

Overall, the present study demonstrates the value of digital image analysis workflows for therapeutic assessment in preclinical in vivo models and subsequent tissue-based disease diagnosis and prognosis. Moreover, the work carried out herein evidences the wide spectrum of possibilities that digital pathology image analysis opens up for the study of TME components to predict disease outcome and precision medicine.

5. Conclusions

In this study, we generated automated digital image analysis pipelines that can be used for standardized quantification of biomarkers in WSIs, thus enabling high throughput analysis at both sample and cellular levels and avoiding intra- and interobserver variability. In total, we were able to analyze 4262407 cells from 16 samples. Furthermore, with this approach biomarkers are assessed in the whole sample, tackling the issue of intratumor heterogeneity that pathologists face when assessing tumor biomarkers. Lastly, we have defined an objective and novel method to define the center and periphery of samples. This could help to perform analyses from a spatial perspective, which may facilitate the identification of potential biomarkers and/or improve their clinical value.

Author contributions

Conceptualization, R.N.; methodology, M.S., I.V.-M., I.N., M.S.-S. and R.B.-P.; software, M.S. and I.V.-M.; validation, S.N. and R.N.; formal analysis, M.S.; data curation, M.S. and I.V.-M.; writing—original draft preparation, M.S.; writing—review and editing, M.S., I.V.-M., I.N., M.S.-S., R.B.-P., S.N., and R.N.; supervision, R.N. All authors have read and agreed to the published version of the manuscript.

Funding

This work was supported by ISCIII (FIS) and ERDF (European Regional Development Fund) [grant number PI20/01107]; CIBERONC [contract CB16/12/00484]; and Fundación Neuroblastoma [PRV/00166]. The APC was funded by ISCIII (FIS) and ERDF (European Regional Development Fund) [grant number PI20/01107]. M.S. was funded by CIBERONC (contract CB16/12/00484) cofunded by ERDF funds. I.V.-M. was funded by Spanish University Ministry [grant FPU20/05344].

Institutional review board statement

The animal study protocol was approved by the Institutional Ethics Committee of Universitat de València (reference 2021/VSC/PEA/0052, 26/02/2021).

Simple summary

In recent years, digital pathology approaches have gained importance in precision medicine as they allow a robust analysis of the tumor microenvironment, aiding the identification of novel biomarkers that enable a better stratification of patients and therapeutic assessment. With the aim of demonstrating that standardized digital detection of tumor microenvironment components could enable more precise prognosis or risk stratification, we generated pipelines for the detection of components of the extracellular matrix of neuroblastoma. Subsequently, we focus on the need of its standardization to assess the efficacy of extracellular matrix targeted therapies. The current work reinforces the importance of digital image analysis workflows for the analysis of clinically relevant biomarkers and therapeutic assessment in cancer, using high-risk neuroblastoma as a model for the application of digital pathology.

Declaration of competing interest

None Declared. The funders had no role in the design of the study; in the collection, analyses, or interpretation of data; in the writing of the manuscript; or in the decision to publish the results.

Acknowledgments

The authors thank Kathryn Davies for English corrections.

Appendix A. Supplementary Materials and Methods

Appendix A.1. Animal care

As transgenic, immunosuppressed, knock-out animals, RAG1−/− (B6.129S7-Rag1tm1Mom/J) VN−/− (B6.129S2 (D2)-Vtntm1Dgi/J) mice were stored under SPF (Specific Pathogen Free) conditions and were housed in cages with individual and filtered ventilation. Mice were exposed to light and dark cycles of 12 h each, and food and water supply was ad. ibitum.

Appendix A.2. Cell inoculation

For SK-N-BE (2) cell inoculation in RAG1−/− and VN−/− mice (n = 29), cells were briefly tripsinized (Bio-Rad Laboratories) for 5 min at 5% CO2 and 37–C atmosphere. Trypsin was inactivated with culture medium, the solution was centrifuged, and the pellet resuspended again with new culture medium. We performed the trypan blue (Bio-Rad Laboratories) viability test. Once the number of living cells was

established, the solution was centrifuged again and the pellet was resuspended in Dulbecco's phosphate-buffered saline (Gibco, Thermo Fisher Scientific Inc. Waltham, MA, USA). The cells were mixed with Matrigel (Corning, Cultek S.L.U, Barcelona, Spain) in a 2:1 proportion to obtain a solution with $2x10^6$ cells in a final volume of 100 μl.

Appendix A.3. Sample collection

Two days after the last treatment administration, animals were sedated with isofluorane (2–3%). Subsequently, a transcardiac puncture was performed to extract approximately 1 mL of blood, which was collected in tubes with EDTA. After blood extraction, animals were euthanized by cervical dislocation. Tumors were collected, measured and photographed. Tumors with a manageable size were divided into two halves, one stored in IMDM culture medium with 1% penicillin-streptomycin and the other fixed by immersion in 4% PFA. If tumor size was not sufficient, they were directly fixed by immersion in PFA. Paraffin embedding and paraffin block assembly were automated with LeicaTP1020 (Leica Microsystems; Wetzlas, Germany) and Leica EG1150H (Leica Microsystems, Wetzlas, Germany), respectively. After, 3-μm sections were cut (Leica RM2145 microtome, Leica Microsystems, Wetzlas, Germany).

Appendix B. Scripts for Digital Image Analysis

The generated and used scripts are available at: https://github.com/LabPatoMolUV/Morphology-tools-VN-alphaVbeta3.

Appendix C. Supplementary data

Supplementary data to this article can be found online at https://doi.org/10.1016/j.compbiomed.2023.107364.

References

[1] N.M. Anderson, M.C. Simon, The tumor microenvironment, Curr. Biol.: CB 30 (16) (2020) R921–R925, https://doi.org/10.1016/j.cub.2020.06.081.

[2] J. Huang, L. Zhang, D. Wan, L. Zhou, S. Zheng, S. Lin, Y. Qiao, Extracellular matrix and its therapeutic potential for cancer treatment, Signal Transduct. Targeted Ther. 6 (1) (2021) 153, https://doi.org/10.1038/s41392-021-00544-0.

[3] d. Seiffert, Constitutive and regulated expression of vitronectin, Histol. Histopathol. 12 (3) (1997) 787–797.

[4] Y. Chu, J.C. Bucci, C.B. Peterson, Identification of a PAI-1-binding site within an intrinsically disordered region of vitronectin, Protein Sci. : Publ. Protein Soc. 29 (2) (2020) 494–508, https://doi.org/10.1002/pro.3770.

[5] L. Heyman, J. Leroy-Dudal, J. Fernandes, D. Seyer, S. Dutoit, F. Carreiras, Mesothelial vitronectin stimulates migration of ovarian cancer cells, Cell Biol. Int. 34 (5) (2010) 493–502, https://doi.org/10.1042/CBI20090331.

[6] W. Zhu, W. Li, G. Yang, C. Fu, G. Jiang, Q. Hu, Vitronectin silencing inhibits hepatocellular carcinoma in vitro and in vivo, Future Oncol. 11 (2) (2015) 251–258, https://doi.org/10.2217/fon.14.202.

[7] J.H. Uhm, N.P. Dooley, A.P. Kyritsis, J.S. Rao, C.L. Gladson, Vitronectin, a glioma-derived extracellular matrix protein, protects tumor cells from apoptotic death, Clin. Cancer Res.: Off. J. Am. Associat. Cancer Res. 5 (6) (1999) 1587–1594.

[8] F. Carreiras, S. Cruet, C. Staedel, F. Sichel, P. Gauduchon, Human ovarian adenocarcinoma cells synthesize vitronectin and use it to organize their adhesion, Gynecol. Oncol. 72 (3) (1999) 312–322, https://doi.org/10.1006/gyno.1998.5262.

[9] B.R. Tomasini-Johansson, C. Sundberg, G. Lindmark, J.O. Gailit, K. Rubin, Vitronectin in colorectal adenocarcinoma–synthesis by stromal cells in culture, Exp. Cell Res. 214 (1) (1994) 303–312, https://doi.org/10.1006/excr.1994.1262.

[10] R.L. Gomez, S. Ibragimova, R. Ramachandran, A. Philpott, F.R. Ali, Tumoral heterogeneity in neuroblastoma. Biochimica et biophysica acta, Rev. Cancer 1877 (6) (2022), 188805, https://doi.org/10.1016/j.bbcan.2022.188805.

[11] E.A. Newman, S. Abdessalam, J.H. Aldrink, M. Austin, T.E. Heaton, J. Bruny, P. Ehrlich, R. Dasgupta, R.M. Baertschiger, T.B. Lautz, D.S. Rhee, M. R. Langham Jr., M.M. Malek, R.L. Meyers, J.D. Nathan, B.R. Weil, S. Polites, M. B. Madonna, APSA Cancer committee, Update on neuroblastoma, J. Pediatr. Surg. 54 (3) (2019) 383–389, https://doi.org/10.1016/j.jpedsurg.2018.09.004.

[12] R. Burgos-Panadero, S.H. el Moukhtari, I. Noguera, C. Rodríguez-Nogales, S. Martín-Vañó, P. Vicente-Munuera, A. Cañete, S. Navarro, M.J. Blanco-Prieto, R. Noguera, Unraveling the extracellular matrix-tumor cell interactions to aid better targeted therapies for neuroblastoma, Int. J. Pharm. 608 (2021), 121058, https://doi.org/10.1016/J.IJPHARM.2021.121058.

[13] R. Burgos-Panadero, I. Noguera, A. Cañete, S. Navarro, R. Noguera, Vitronectin as a molecular player of the tumor microenvironment in neuroblastoma, BMC Cancer 19 (1) (2019) 479, https://doi.org/10.1186/s12885-019-5693-2.

[14] J.D. Pallua, A. Brunner, B. Zelger, M. Schirmer, J. Haybaeck, The future of pathology is digital, Pathol. Res. Pract. 216 (9) (2020), 153040, https://doi.org/10.1016/j.prp.2020.153040.

[15] S.W. Jahn, M. Plass, F. Moinfar, Digital pathology: advantages, limitations and emerging perspectives, J. Clin. Med. 9 (11) (2020) 3697, https://doi.org/10.3390/jcm9113697.

[16] K. Bera, K.A. Schalper, D.L. Rimm, V. Velcheti, A. Madabhushi, Artificial intelligence in digital pathology - new tools for diagnosis and precision oncology, Nat. Rev. Clin. Oncol. 16 (11) (2019) 703–715, https://doi.org/10.1038/s41571-019-0252-y.

[17] P. Vicente-Munuera, R. Burgos-Panadero, I. Noguera, S. Navarro, R. Noguera, L. M. Escudero, The topology of vitronectin: a complementary feature for neuroblastoma risk classification based on computer-aided detection, Int. J. Cancer 146 (2) (2020) 553–565, https://doi.org/10.1002/ijc.32495.

[18] I. Tadeo, A.P. Berbegall, V. Castel, P. García-Miguel, R. Callaghan, S. Påhlman, S. Navarro, R. Noguera, Extracellular matrix composition defines an ultra-high-risk group of neuroblastoma within the high-risk patient cohort, Br. J. Cancer 115 (4) (2016) 480–489, https://doi.org/10.1038/bjc.2016.210.

[19] S.B. Whittle, V. Smith, E. Doherty, S. Zhao, S. McCarty, P.E. Zage, Overview and recent advances in the treatment of neuroblastoma, Expet Rev. Anticancer Ther. 17 (4) (2017) 369–386, https://doi.org/10.1080/14737140.2017.1285230.

[20] I. Horwacik, The extracellular matrix and neuroblastoma cell communication-A complex interplay and its therapeutic implications, Cells 11 (19) (2022) 3172, https://doi.org/10.3390/cells11193172.

[21] F. Liu, Q. Wu, Z. Dong, K. Liu, Integrins in cancer: emerging mechanisms and therapeutic opportunities, Pharmacol. Ther. 247 (2023), 108458, https://doi.org/10.1016/j.pharmthera.2023.108458.

[22] C. Mas-Moruno, F. Rechenmacher, H. Kessler, Cilengitide: the first anti-angiogenic small molecule drug candidate design, synthesis and clinical evaluation, Anti Cancer Agents Med. Chem. 10 (10) (2010) 753–768, https://doi.org/10.2174/187152010794728639.

[23] O.L. Chinot, Cilengitide in glioblastoma: when did it fail? The Lancet, Oncology 15 (10) (2014) 1044–1045, https://doi.org/10.1016/S1470-2045(14)70403-6.

[24] P. Bankhead, M.B. Loughrey, J.A. Fernández, Y. Dombrowski, D.G. McArt, P. D. Dunne, S. McQuaid, R.T. Gray, L.J. Murray, H.G. Coleman, J.A. James, M. Salto-Tellez, P.W. Hamilton, QuPath: open source software for digital pathology image analysis, Sci. Rep. 7 (1) (2017), 16878, https://doi.org/10.1038/s41598-017-17204-5.

[25] R. Pell, K. Oien, M. Robinson, H. Pitman, N. Rajpoot, J. Rittscher, D. Snead, C. Verrill, UK National Cancer Research Institute (NCRI) Cellular-Molecular Pathology (CM-Path) quality assurance working group, The use of digital pathology and image analysis in clinical trials. The journal of pathology, Clin. Res. 5 (2) (2019) 81–90, https://doi.org/10.1002/cjp2.127.

[26] V. Baxi, R. Edwards, M. Montalto, S. Saha, Digital pathology and artificial intelligence in translational medicine and clinical practice, Mod. Pathol. : Off.J. United States Canad.Academy of Pathol. Inc. 35 (1) (2022) 23–32, https://doi.org/10.1038/s41379-021-00919-2.

[27] Y. Song, K. Kang, I. Kim, T.J. Kim, Pathological digital biomarkers: validation and application, Appl. Sci. 12 (19) (2022), https://doi.org/10.3390/app12199823.

[28] J. Zou, E. Wang, Cancer biomarker discovery for precision medicine: new progress, Curr. Med. Chem. 26 (42) (2019) 7655–7671, https://doi.org/10.2174/0929867325666180718164712.

[29] J. Shang, F. Wang, P. Chen, X. Wang, F. Ding, S. Liu, Q. Zhao, Co-Expression network analysis identified COL8A1 is associated with the progression and prognosis in human colon adenocarcinoma, Dig. Dis. Sci. 63 (5) (2018) 1219–1228, https://doi.org/10.1007/s10620-018-4996-5.

[30] M. Romagnoli, N.D. Mineva, M. Polmear, C. Conrad, S. Srinivasan, D. Loussouarn, S. Barillé-Nion, I. Georgakoudi, Á. Dagg, E.W. McDermott, M.J. Duffy, P. M. McGowan, U. Schlomann, M. Parsons, J.W. Bartsch, G.E. Sonenshein, ADAM8 expression in invasive breast cancer promotes tumor dissemination and metastasis, EMBO Mol. Med. 6 (2) (2014) 278–294, https://doi.org/10.1002/emmm.201303373.

[31] L. Dai, J. Mugaanyi, X. Cai, M. Dong, C. Lu, C. Lu, Comprehensive bioinformatic analysis of MMP1 in hepatocellular carcinoma and establishment of relevant prognostic model, Sci. Rep. 12 (1) (2022), 13639, https://doi.org/10.1038/s41598-022-17954-x.

[32] S.L. Cohn, A.D. Pearson, W.B. London, T. Monclair, P.F. Ambros, G.M. Brodeur, A. Faldum, B. Hero, T. Iehara, D. Machin, V. Mosseri, T. Simon, A. Garaventa, V. Castel, K.K. Matthay, INRG Task Force, The international neuroblastoma risk group (INRG) classification system: an INRG task force report, J. Clin. Oncol.: Off.J. Am.Soc.Clin.Oncol. 27 (2) (2009) 289–297, https://doi.org/10.1200/JCO.2008.16.6785.

[33] V. Smith, J. Foster, High-risk neuroblastoma treatment review, Children 5 (9) (2018) 114, https://doi.org/10.3390/children5090114.

[34] M.H. Chen, C. Lu, J. Sun, X.D. Chen, J.X. Dai, J.Y. Cai, X.L. Chen, Diagnostic and prognostic value of serum vitronectin levels in human glioma, J. Neurol. Sci. 371 (2016) 54–59, https://doi.org/10.1016/j.jns.2016.10.022.

[35] A.F. Radwan, O.E. Ismael, A. Fawzy, H.O. El-Mesallamy, Evaluation of serum integrin αvβ3 & vitronectin in the early diagnosis of breast cancer, Clin. Lab. 65 (7) (2019), https://doi.org/10.7754/Clin.Lab.2019.181219, 10.7754/Clin.Lab.2019.181219.

[36] K. Shi, R.L. Lan, X. Tao, C.Y. Wu, H.F. Hong, J.H. Lin, Vitronectin significantly influences prognosis in osteosarcoma, Int. J. Clin. Exp. Pathol. 8 (9) (2015) 11364–11371.

[37] I. Ortega-Martínez, J. Gardeazabal, A. Erramuzpe, A. Sanchez-Diez, J. Cortés, M. D. García-Vázquez, G. Pérez-Yarza, R. Izu, J. Luís Díaz-Ramón, I.M. de la Fuente, A. Asumendi, M.D. Boyano, Vitronectin and dermcidin serum levels predict the metastatic progression of AJCC I-II early-stage melanoma, Int. J. Cancer 139 (7) (2016) 1598–1607, https://doi.org/10.1002/ijc.30202.

[38] C. Gong, H. Hong, J. Xie, Y. Xue, Y. Huang, D. Zhang, Over-expression of vitronectin correlates with impaired survival in gastric cancers, Medicine 100 (31) (2021), e26766, https://doi.org/10.1097/MD.0000000000026766.

[39] K.S. Chan, S.M. Cheung, N. Senn, E. Husain, Y. Masannat, S. Heys, J. He, Peri-tumoural spatial distribution of lipid composition and tubule formation in breast cancer, BMC Cancer 22 (1) (2022) 285, https://doi.org/10.1186/s12885-022-09362-1.

[40] X. Zheng, A. Weigert, S. Reu, S. Guenther, S. Mansouri, B. Bassaly, S. Gattenlöhner, F. Grimminger, S. Pullamsetti, W. Seeger, H. Winter, R. Savai, Spatial density and distribution of tumor-associated macrophages predict survival in non-small cell lung carcinoma, Cancer Res. 80 (20) (2020) 4414–4425, https://doi.org/10.1158/0008-5472.CAN-20-0069.

[41] S. Park, C.Y. Ock, H. Kim, S. Pereira, S. Park, M. Ma, S. Choi, S. Kim, S. Shin, B. J. Aum, K. Paeng, D. Yoo, H. Cha, S. Park, K.J. Suh, H.A. Jung, S.H. Kim, Y.J. Kim, J.M. Sun, J.H. Chung, S.H. Lee, Artificial intelligence-powered spatial analysis of tumor-infiltrating lymphocytes as complementary biomarker for immune checkpoint inhibition in non-small-cell lung cancer, J. Clin. Oncol. : Off.J. Am.Soc. Clin.Oncol. 40 (17) (2022) 1916–1928, https://doi.org/10.1200/JCO.21.02010.

[42] C. Lau, B. Kalantari, K.P. Batts, L.D. Ferrell, S.L. Nyberg, R.P. Graham, R. K. Moreira, The Voronoi theory of the normal liver lobular architecture and its applicability in hepatic zonation, Sci. Rep. 11 (1) (2021) 9343, https://doi.org/10.1038/s41598-021-88699-2.

[43] D. Sánchez-Gutiérrez, M. Tozluoglu, J.D. Barry, A. Pascual, Y. Mao, L.M. Escudero, Fundamental physical cellular constraints drive self-organization of tissues, EMBO J. 35 (1) (2016) 77–88, https://doi.org/10.15252/embj.201592374.

[44] M.K.K. Niazi, A.V. Parwani, M.N. Gurcan, Digital pathology and artificial intelligence, Lancet Oncol. 20 (5) (2019) e253–e261, https://doi.org/10.1016/S1470-2045(19)30154-8.

[45] L. Sancey, S. Lucie, E. Garanger, G. Elisabeth, S. Foillard, F. Stéphanie, G. Schoehn, S. Guy, A. Hurbin, H. Amandine, C. Albiges-Rizo, A.R. Corinne, D. Boturyn, B. Didier, C. Souchier, S. Catherine, A. Grichine, G. Alexeï, P. Dumy, D. Pascal, C. Jean-Luc, Clustering and internalization of integrin alphavbeta3 with a tetrameric RGD-synthetic peptide, Mol. Ther.: J. Am. Soc. Gene Ther. 17 (5) (2009) 837–843, https://doi.org/10.1038/mt.2009.29.

[46] S. Edwards, P.F. Lalor, C. Tuncer, D.H. Adams, Vitronectin in human hepatic tumours contributes to the recruitment of lymphocytes in an alpha v beta3-independent manner, Br. J. Cancer 95 (11) (2006) 1545–1554, https://doi.org/10.1038/sj.bjc.6603467.

[47] P. Leblond, A. Dewitte, F. Le Tinier, C. Bal-Mahieu, M. Baroncini, T. Sarrazin, E. Lartigau, A. Lansiaux, S. Meignan, Cilengitide targets pediatric glioma and neuroblastoma cells through cell detachment and anoikis induction, Anti Cancer Drugs 24 (8) (2013) 818–825, https://doi.org/10.1097/CAD.0b013e328362edc5.

[48] J. Liu, Q. Chen, L. Feng, Z. Liu, Nanomedicine for tumor microenvironment modulation and cancer treatment enhancement, Nano Today 21 (2018) 55–73, https://doi.org/10.1016/j.nantod.2018.06.008. Elsevier B.V.